Marine Geology 341 (2013) 58–67

Contents lists available at SciVerse ScienceDirect

Marine Geology

journal homepage: www.elsevier.com/locate/margeo

Modification of mudstone fabric and pore structure as a result of slope failure: Ursa Basin, Gulf of Mexico

Ruarri J. Day-Stirrat [a,*], Peter B. Flemings [b], Yao You [b], Ben A. van der Pluijm [c]

[a] Bureau of Economic Geology, Jackson School of Geosciences, The University of Texas at Austin, University Station, Box X, Austin, TX 78713, USA
[b] Jackson School of Geosciences, The University of Texas at Austin, University Station, Box X, Austin, TX 78713, USA
[c] Department of Geological Sciences, University of Michigan, C.C. Little Building, 425 E. University Ave., Ann Arbor, MI 48109-1063, USA

ARTICLE INFO

Article history:
Received 20 December 2012
Received in revised form 9 May 2013
Accepted 11 May 2013
Available online 20 May 2013

Communicated by D.J.W. Piper

Keywords:
mass transport deposit
anisotropy
mudstone porosity
fabric

ABSTRACT

Mud-rich mass transport deposits (MTDs) have a microfabric that is significantly different from bounding non-deformed mudstones at similar depths in the first 200 m of burial. Core samples from the Integrated Ocean Drilling Program Expedition 308, Ursa Basin, Gulf of Mexico sample many well identified MTDs. These MTD mudstones have higher clay mineral fabric intensities than compositional equivalent mudstones either at a given porosity or a given depth. Clay mineral fabric intensity was quantified using high resolution X-ray texture goniometry and confirmed by visual inspection on backscattered electron micrographs imaged on argon-ion milled surfaces. Enhanced clay-mineral fabric intensities in MTD mudstones are interpreted to result from remolding and shearing after mass movement, where the initially deposited clay mineral flocs have been mechanically disaggregated and physio-chemical forces of attraction overcome. Recognition of enhanced microfabrics has important implications for seismic anisotropy as well as for shallow fluid flow.
© 2013 Elsevier B.V. All rights reserved.

1. Introduction

Mass transport deposits (MTDs) may comprise 50% of the rock record in deep marine continental margins (McMurtry et al., 2004; Garziglia et al., 2008). MTDs are sedimentary deposits that result from slides, slumps and debris flows (Stow, 1986; Weimer and Shipp, 2004); and do not result from turbidite flows (Moscardelli et al., 2006 and references therein). MTDs record slope failure and they can occur in association with tsunamis (Tappin et al., 2001; Fryer et al., 2004; Dan et al., 2007). MTDs are a shallow drilling hazards in hydrocarbon exploration (e.g. Piper et al., 1997; Shipp et al., 2004 and references therein) as shallow overpressures may result and cause sediment flow near to a rig caisson.

Mud-rich MTDs are commonly identified by their strong basal seismic reflector (e.g. Moscardelli and Wood, 2008; Sawyer et al., 2009; Dugan, 2012), with the MTD itself being a low-amplitude zone and the underlying unit a high-amplitude zone. Outcrop studies (Pickering and Corregidor, 2005) and core-based research (Jenner et al., 2007; Sawyer et al., 2009) have begun to tie MTD lithological and petrophysical behavior to the seismic response (Moscardelli and Wood, 2008; Tripsanas et al., 2008) with Shipp et al. (2004) describing how MTDs have lower porosity than surrounding, non-deformed sediments. More recently, Integrated Ocean Drilling Program (IODP) Expedition 308 documented a sediment density increase in repeated MTDs in the Ursa Basin (Sawyer et al., 2009; Dugan, 2012) and Meissl et al. (2010) described the reduction in permeability and decrease in compressibility.

Shipp et al. (2004) and Sawyer et al. (2009) proposed that the sediment density increase observed is due to a process called remolding: a shearing process at constant void ratio that results in breakdown of the original soil structure (Mitchell and Soga, 2005) as a result of slumping and sediment movement rather than initial depositional processes. This breakdown in original structure occurred during a slope failure. The precursor clay-rich sediment presumably had a random orientation of clay particles (O'Brien, 1970, 1971) but during slope failure mechanical remolding took place, altering the sediment microfabric. Laboratory uniaxial consolidation at equivalent vertical effect stress on intact and remolded samples (Skempton, 1970; Burland, 1990) found lower porosity in remolded samples.

We further explore the sediment density increase observed within MTDs through an analysis of the microfabric and pore modification of MTDs. We quantify how sediment mass movement modifies the microfabric by shear and aligns clay mineral in a manner similar to how clay minerals are aligned in fault gouge (Solum et al., 2003; Solum et al., 2005; Haines et al., 2009). Cores from IODP Expedition 308 provide an excellent opportunity to explore the microfabric of mud-rich MTDs. We first characterize the mineralogy and grain size distributions of MTD mudstone and mudstones from the Ursa Basin. We show that clay minerals are more aligned in MTD mudstone than in bounding intact sediment using high resolution X-ray texture

* Corresponding author at: Shell International Exploration and Production, Shell Technology Center — Houston, 3333 Highway 6 South, Houston, TX, 77082, USA. Tel.: +1 5125061678.
E-mail address: ruarri.day-stirrat@shell.com (R.J. Day-Stirrat).

0025-3227/$ – see front matter © 2013 Elsevier B.V. All rights reserved.
http://dx.doi.org/10.1016/j.margeo.2013.05.003

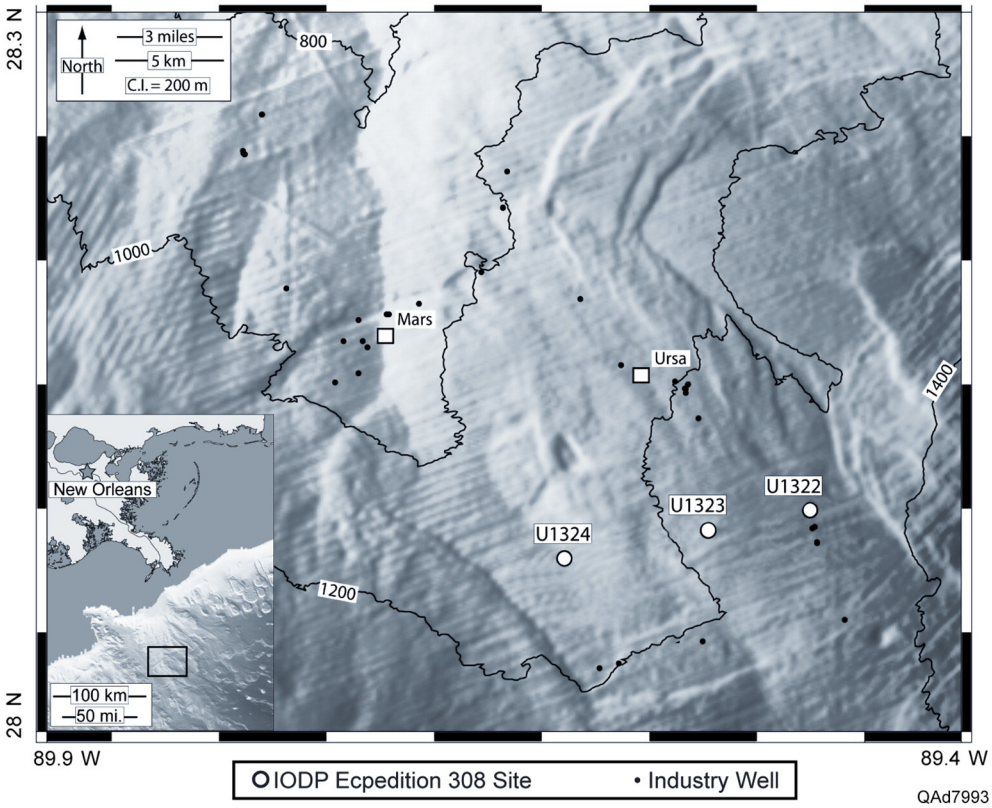

Fig. 1. The location of the Ursa Basin on the continental slope in water depths of ~1000 m. The Ursa Basin in the Gulf of Mexico and the locations of IODP Expedition Leg 308 drill Sites U1234, U1323 and U1322 relative to oil and gas drilling platforms Mars and Ursa, black dots are industry wells.

goniometry (van der Pluijm et al., 1994). We then show these fabrics in backscattered electron images using argon-ion milled sample surfaces. With the aid of these images and mercury injection capillary pressure (MICP) data we find that MTD mudstones have distinct pore throat size distributions relative to mudstones consolidated by only a change in vertical effective stress. Through this analysis we can describe how MTD mudstones could have enhanced sealing qualities, low permeabilities and potentially enhance permeability anisotropy.

2. Materials and methods

2.1. Ursa region samples

Whole cores from IODP Expedition 308 Site 1324 and Site 1322 (Fig. 1) provide the samples for this study. Mass transport deposits (MTDs) are abundant at Ursa and their presence and identification are well defined (Sawyer et al., 2009). Samples range from depths

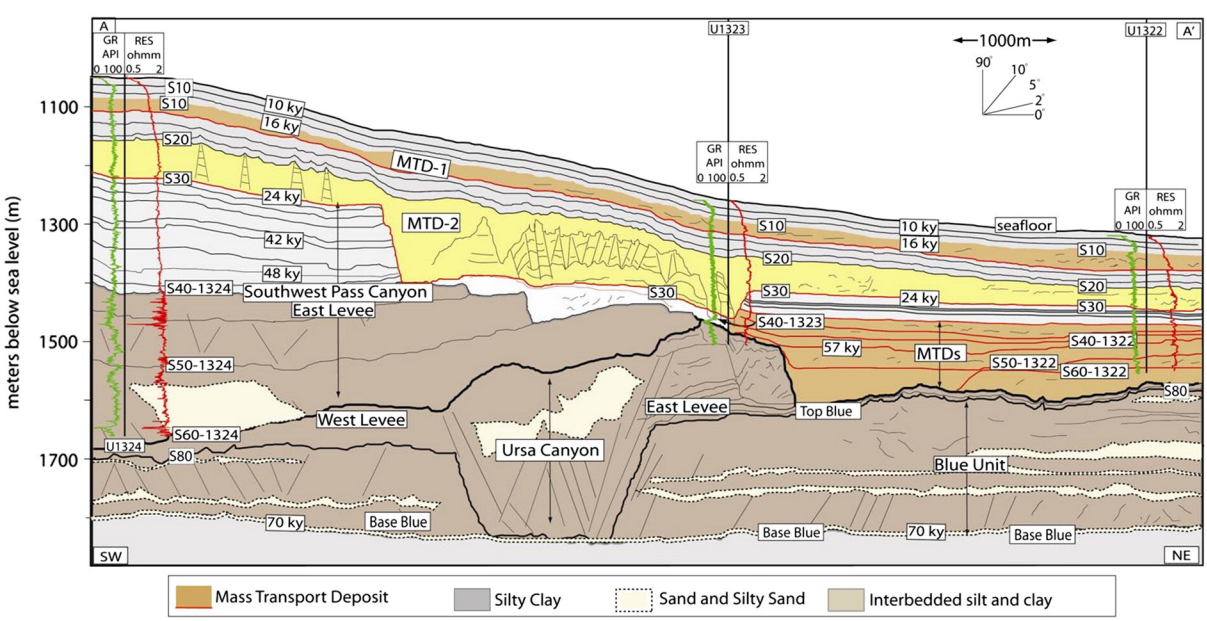

Fig. 2. Interpreted seismic line showing locations of Mass Transport Deposits (MTDs) through Sites U1324, U1323 and U1322. Major MTDs (1 and 2) are marked. Modified from interpretation by Sawyer et al. (2009).

Table 1
Physical properties at Ursa Sites U1322 and U1324.

Sample	U1322 B 005H 07 WR	U1324 B 006H 07 WR	U1322 D 002H 02 WR	U1322 D 002H 04 WR	U1322 D 003H 04 WR	U1322 B 013H 06 WR	U1324 B 013H 07 WR	U1322 B 015H 01 WR	U1324 B 015H 06 WR	U1322 B 018H 06	U1324 B 020H 06 WR	U1322 B 025H 06 WR	U1322 B 026H 02 WR	U1322 B 029H 01 WR	U1324 B 034H 06	U1324 B 044H 01 WR	U1324 B 055X 04	U1324 B 070X 06	U1324 B 071X 06
Depth [mbsf]	41.8	51.2	71.5	74.5	104.5	115.2	117.3	126.1	135.7	149.9	178.6	201.7	213	228.4	282.5	354.1	425.7	570	579.6
MTD	Yes	Yes	No	No	Yes	Yes	Yes	No	Yes	No	No	No	Yes	Yes	No	No	No	No	No
% <2 μm	60	64	67	62	57	63	60	62	50	61	63	64	58	64	69	70	63	59	20
Void ratio [e] from moisture and density	1.44	1.44	1.10	1.24	0.85	0.82	0.79	1.00	0.85	0.83	0.86	0.72	0.82		0.75	0.74	0.64	0.60	0.69
[n] Porosity [%] moisture and density	0.59	0.59	0.52	0.55	0.46	0.45	0.44	0.50	0.46	0.46	0.46	0.42	0.45		0.43	0.42	0.39	0.38	0.41
[σv'] Vertical effective stress [MPa]	0.10	0.14	0.24	0.25	0.37	0.43	0.44	0.41	0.54	0.48	0.90	0.96	1.03	1.14	1.72	2.28	2.84	3.98	4.05
Porosity [n] from MICP	0.39	0.49	0.46	0.49	0.36	0.33	0.32	0.36	0.34	0.35	0.37	0.35	0.35	0.36	0.34	0.40	0.32	0.33	0.33
Cut off radius (nm)	1822	4373	2733	2733	547	156	1822	547	199	729	2733	547	273	547	364	729	547	729	10,933
Mean porosity [rmean] (nm)	150	171	110	156	42	32	168	48	45	50	64	40	37	48	25	51	56	37	1146
Pore throat radius at 10% Hg saturation [r10%] (nm)	326	345	185	303	71	58	424	82	74	83	94	69	63	78	48	87	114	62	2733
Displacement pressure [psi]	332	313	586	357	1528	1880	255	1323	1455	1304	1148	1560	1704	1382	2274	1240	948	1740	40
P10% for oil (psi)	31	29	55	34	143	176	24	124	137	122	108	146	160	130	213	116	89	163	4
P10% for gas (psi)	41	39	72	44	188	232	31	163	179	161	142	192	210	170	280	153	117	215	5
Calculated oil column height (m)	95	90	168	103	439	540	73	380	418	374	329	448	489	397	653	356	272	499	11
Calculated gas column height (m)	33	31	58	36	152	187	25	132	145	130	114	155	170	138	227	124	94	173	4
Max. pole density m.r.d. [illite–smectite]	2.23	2.86	3.00	3.00	3.62	2.93	3.34	2.49	3.65	2.50	2.53	3.01	3.41		2.57	2.71	2.77	3.45	1.90
Max. pole density m.r.d. [illite–smectite]	1.89	2.94	3.08	2.88	4.03	2.84	3.22	2.40	3.52	2.31	2.61	2.97	3.36		2.50	3.00		3.17	
Max. pole density m.r.d. [illite–smectite]		3.02		2.42	3.76			2.64	3.41		2.68		3.51		2.43	2.91			
Max. pole density m.r.d. [illite–smectite]		3.42		2.24	3.33			2.59	3.61				3.29						
Max. pole density m.r.d. [illite–smectite]		2.97			3.28			2.68	3.68										
Max. pole density m.r.d. [illite–smectite]								2.55											
Max. pole density m.r.d. [illite–smectite]								2.65											
Max. pole density m.r.d. [illite–smectite]								2.51											
Max. pole density m.r.d. [illite–smectite]								2.62											
Max pole density m.r.d. [kaolinite + chlorite]	1.88	2.8		2.94	3.43	2.93	3.43	1.71	3.61	2.19	2.47		3.28		2.46	2.74	2.6	3.04	
Max pole density m.r.d. [kaolinite + chlorite]		3.42		3.94	4.09	2.68		2.63	3.3	2.58	2.56		3.43			3.05		3.62	
Max pole density m.r.d. [kaolinite + chlorite]		2.97						2.41	3.11	2.58	2.56					2.92		3.61	
Max pole density m.r.d. [kaolinite + chlorite]								2.51	3.65	2.19	2.47					3.04		3.04	
Max pole density m.r.d. [kaolinite + chlorite]								2.52	3.26							2.74			
Max pole density m.r.d. [kaolinite + chlorite]								1.71											
Max pole density m.r.d. [kaolinite + chlorite]								2.62											

of 41.8 to 579.6 mbsf (Fig. 2, Table 1). In order to achieve this coverage, both Sites U1324 and U1322 were sampled and samples identified as coming from MTDs augment the mudstones from the same wells (Figs. 3 and 4) previously characterized (Day-Stirrat et al., 2012) in terms of their microfabric. Sediments in Ursa cores have a similar composition and depositional history at both Sites U1322 and U1324 (Flemings et al., 2006; Sawyer et al., 2009; Day-Stirrat et al., 2012).

2.2. Pore throat size

Pore throat size distributions on 19 samples from Sites U1324 (9) and U1322 (10) were determined by mercury porosimetry. For each analysis a block (weighing approximately 1 g) of mudstone sample was submerged in liquid nitrogen for 5 min before being freeze dried (Delage and Lefebvre, 1984) for 24 h, then dried in an oven at 105 °C for a further 24 h. Freeze-drying effectively eliminates surface tension forces and, therefore, no shrinkage of the sample by dehydration of illite–smectite is expected in sample preparation (Romero and Simms, 2008). The porosity of each sample was calculated from dry bulk density (ρ_d) and grain density (G_s):

$$\varphi = 1 - \frac{\rho_d}{G_s}. \quad (1)$$

Grain density was determined previously for Ursa region samples and was generally near 2.70 g/cm^3 (Sawyer et al., 2008). Therefore, grain density was assumed to be 2.70 g/cm^3 in the above calculation. Small differences in grain densities relative to the assumed values can increase or decrease porosity by a small amount. Dry bulk density (ρ_d) was calculated from the known mass of the sample after drying and from the bulk volume of the sample measured in the mercury penetrometer.

During mercury intrusion experiments performed on a Micromeritics© Autopore P 9220, mercury is injected at progressively increasing pressures (logarithmical pressure steps to 40,000 psi) into the previously dried and evacuated sample (Arnould et al., 1980; Lowell and Shields, 1984). Mercury pressure is assumed to equal the capillary pressure in the smallest pore throats that the mercury can enter. The radius (r) of the pore throats are thus inferred from the Washburn (1921) equation:

$$r = 2\gamma(\cos\theta)/P. \quad (2)$$

To calculate the pore throat radius (r) from absolute mercury injection pressure (P), it is assumed that the contact angle between mercury and the particle surface (θ) is 141° (e.g. Hildenbrand and Urai, 2003) and surface tension of mercury (γ) is 0.48 N/m. To use Eq. (2) to infer pore throat distribution, all pore throats must be accessible to the mercury as in, for example, a parallel capillary tube model (e.g. Schowalter, 1979; Romero and Simms, 2008).

2.3. Clay mineral preferred orientation

The maximum X-ray diffraction peak close to a d-spacing of 10 Å, corresponding to illite–smectite 001, was analyzed to assess illite–

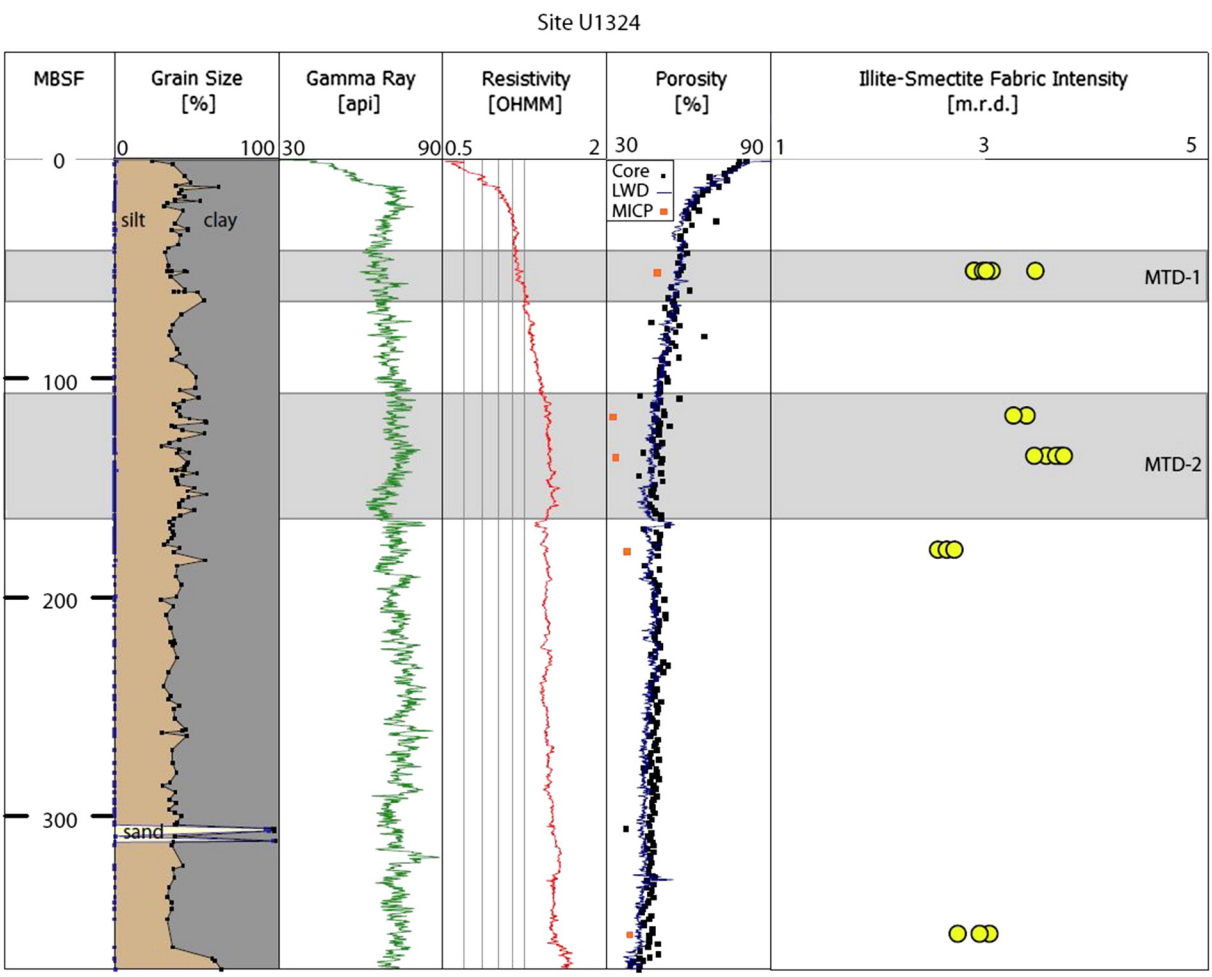

Fig. 3. IODP Site 1324. Depth in meters below sea floor with location of MTD-1 and MTD-2 based on Sawyer et al. (2009). Grain size (%) and gamma-ray log response (gapi units) show no significant changes with depth. Resistivity increases through the MTD zones. Porosity (%) from core (moisture and density), logging (LWD = logging while drilling) and mercury injection (MICP) show a decrease within MTDs. Illite–smectite fabric intensity (maximum pole density) in multiples of a random distribution (m.r.d.).

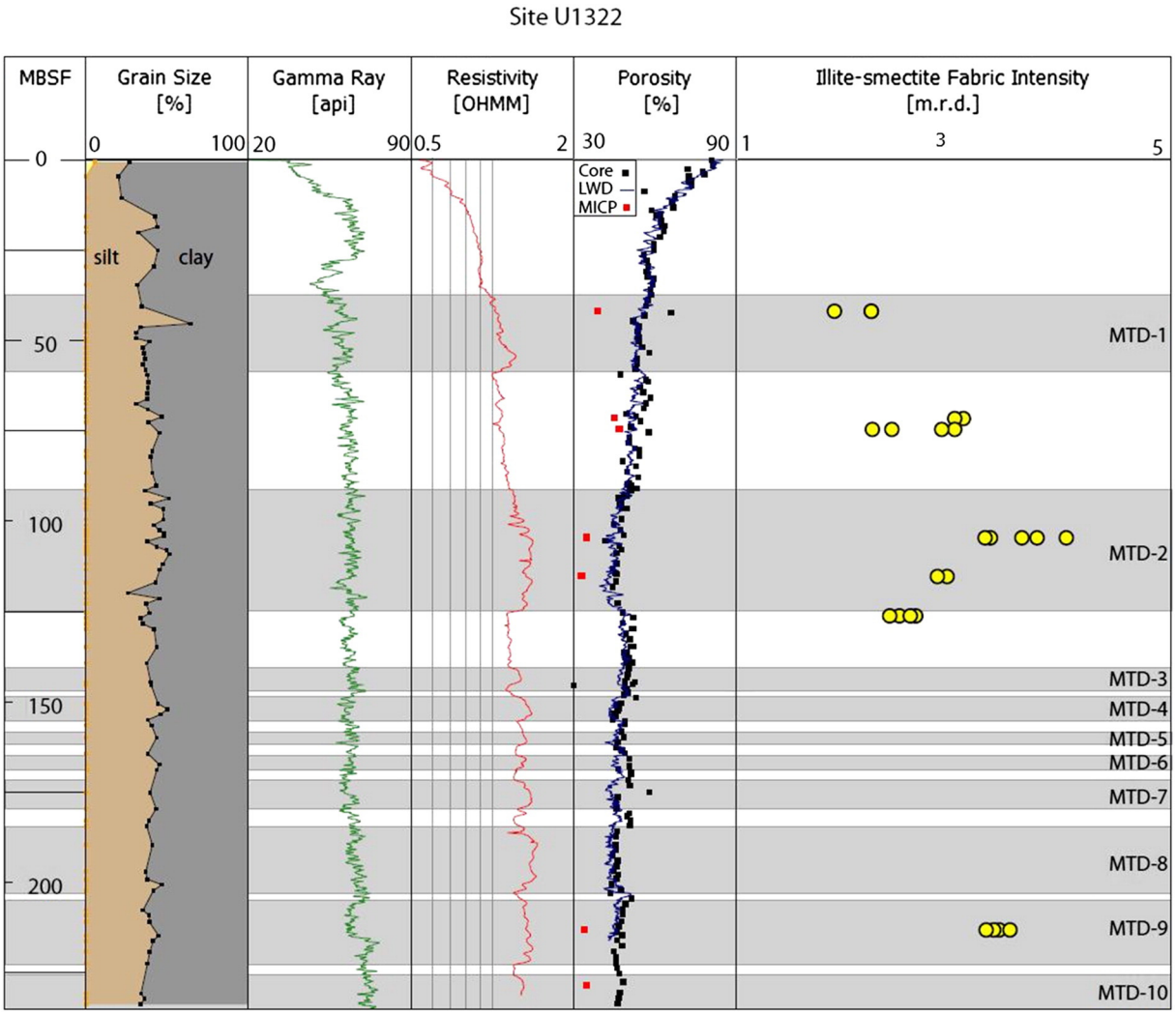

Fig. 4. IODP Site 1322. Depth in meters below sea floor with location of MTD-1 and MTD-2 based on Sawyer et al. (2009), other MTDs are interpreted but do not cross the basin. Grain size (%) and gamma-ray log response (gapi units) show no significant changes with depth. Resistivity increases markedly through the MTD zones and abruptly decreases below. Porosity (%) from core (moisture and density), logging (LWD = logging while drilling) and mercury injection (MICP) show a decrease within MTDs. Illite–smectite fabric intensity (maximum pole density) in multiples of a random distribution (m.r.d.).

smectite preferred orientation on an Enraf-Nonius CAD4 automated single-crystal diffractometer using the high resolution X-ray texture goniometry (HRXTG) method described by van der Pluijm et al. (1994). The 10 Å peak (illite–smectite) was analyzed for all samples and where present a 7 Å peak was analyzed which corresponds to the overlapping 001 peak of kaolinite and 002 peak of chlorite. Data quality was controlled by assessing the lower hemisphere equal area projections of X-ray intensity at different tilt and rotation angles and described only minimal data lost to an unmeasured area (van der Pluijm et al., 1994; Sintubin, 1995; van der Pluijm et al., 1995). The degree of clay mineral preferred orientation is expressed as maximum pole densities in, m.r.d., multiples of a random distribution (Wenk, 1985), in which higher values reflect higher degrees of preferred orientation.

2.4. Pore and particle imaging

A chip of sample was cut for backscattered electron microscopy (BSE). Argon-ion milling produces surfaces, cut approximately perpendicular to bedding, that show only minor topographic relief unrelated to differences in mineral hardness. The argon-ion milling system was operated at an accelerating voltage of 5 to 7 kV and a gun current of ~300 μA. These settings have proven effective at producing relatively flat surfaces for imaging pores (Loucks et al., 2009) and on poorly-consolidated samples (Day-Stirrat et al., 2012). Samples were examined using a Zeiss Supra 40 VP field emission SEM and SE and BSE detectors, at the University of Texas, using an accelerating voltage of 10 kV and a working distance of ~5 mm.

2.5. Grain size

Grain size distributions were analyzed using the standard hydrometer method (ASTM D422-63, 2003). Grain density for the hydrometer analysis was previously determined for Ursa region samples (Sawyer et al., 2008) according to ASTM Standard D854-06 (ASTM, 2007), which is a water pycnometer method. Nineteen grain sizes were determined for this study (Table 1) and augment previous determinations (Sawyer et al., 2008).

3. Results

3.1. Lithology

Grain size, gamma-ray (GR) log response (Sawyer et al., 2009), and mineralogy (John and Adatte, 2009) do not vary significantly within mudstones at Ursa (Figs. 3 and 4). Previously documented

XRD measurements on samples from Ursa show a clay mineralogy dominated by randomly interstratified illite–smectite (Day-Stirrat et al., 2012) but kaolinite and chlorite are also present. Grain sizes are within a fairly narrow range (50–70%, <2 μm) but MTD mudstone samples are marginally coarser grained than mudstone samples (Fig. 5 and Table 1) all samples in this study may be classified as silty clays using the Shepard (1954) nomenclature.

3.2. Porosity

Previously, Long et al. (2011) described the porosity in mudstones at IODP Site U1324 and IODP Site U1322. At Site U1324 (Fig. 3) porosity declines from 80% at the seafloor to 37% at 612 mbsf. Core-derived porosities from moisture and density (MAD) are typically ~2% greater than logging while drilling (LWD) derived porosities (Figs. 3 and 4); this is because the core expands when it is removed from the borehole. In turn, porosity calculated from mercury injection (MICP) is consistently about 5 porosity units lower than Logging While Drilling (LWD) porosity (Fig. 3) (Day-Stirrat et al., 2012). Shrinkage of the sample during storage and transport causes part of this discrepancy. In addition, clay-bound water is interpreted as porosity in both LWD and MAD data. However, this is not pore throat water and cannot be accessed by mercury. Sawyer et al. (2009) noted the decrease in porosity through the MTD zones (Figs. 3 and 4) and it does not follow an effective stress driven porosity reduction.

3.3. Clay mineral preferred orientation

Illite–smectite maximum pole density (in m.r.d.) increases, approximately linearly (Figs. 3 and 4), from ~2.24 at 71.5 mbsf to ~3.45 at 570 mbsf in mudstones (Day-Stirrat et al., 2012). The deepest sample, at 579 mbsf, has a much lower maximum pole density, but is also silt-rich (clay fraction = 20%) (Fig. 3, Table 1). Multiple measurements on the same sample document heterogeneity in the illite–smectite preferred orientation (Fig. 3) on a 1 mm scale, the diameter of the X-ray beam. Regardless, MTD mudstone samples have higher fabric intensities than mudstones at either equivalent depths or porosities (Figs. 3 and 4). At Site U1322 at the base of MTD-2 where the resistivity abruptly reverses and the porosity trend increases, the mudstones in this zone have significantly reduced illite–smectite fabric intensities relative to the MTD samples immediately above (Fig. 4).

3.4. Pore and particle images

Back-scattered electron (BSE) images for two samples (Fig. 6) located at 104.5 mbsf and 178.6 mbsf are representative of the MTD mudstones and mudstones in this study. These samples have a porosity of 36 and 37%, respectively, as measured by the MICP analyses (Fig. 7, Table 1). In a parallel study Day-Stirrat et al. (2012) noted that the largest pores are adjacent to the largest (~5 μm diameter) silt particles and clay particles appear molded onto the surface of a quartz grain (similarly noted by Forsberg and Locat, 2005) with an associated rim of clay micropores. Smaller pores are also preserved between clay-sized particles. Silt-sized grains bridge smaller grains and form stress arches providing a location where porosity may be preserved. On a visual inspection the clay minerals in the MTD sample are significantly more aligned (parallel to the base of the image) than those in the mudstone sample. This observation is consistent with the quantifications for preferred orientation given above.

3.5. Pore throat size

Three samples are selected for comparison of their responses to mercury injection (Fig. 7). First, an MTD mudstone (36% porosity, 104.5 mbsf) is compared to a non-MTD mudstone (37% porosity, 178.6 mbsf). Here, the comparison (Fig. 7A and B) deals with the different processes that caused the samples to have the same porosity (note that depths are different). Second, an MTD mudstone (36% porosity, 104.5 mbsf) is compared to a conventional mudstone (49% porosity, 51.2 mbsf) from shallow burial positions where the 13% porosity difference between samples cannot be simply explained by disequilibrium compaction alone (Fig. 7C and D). Third, two mudstones (Fig. 7E and F) only under the influence of vertical effective stress (σ_v') change (Day-Stirrat et al., 2012) are compared (51.2 mbsf to 178.6 mbsf; σ_v' 0.24 and 0.90 MPa).

In the first case (Fig. 7A and B), mercury intrusion curves appear quite similar however the MTD mudstone has a slightly higher

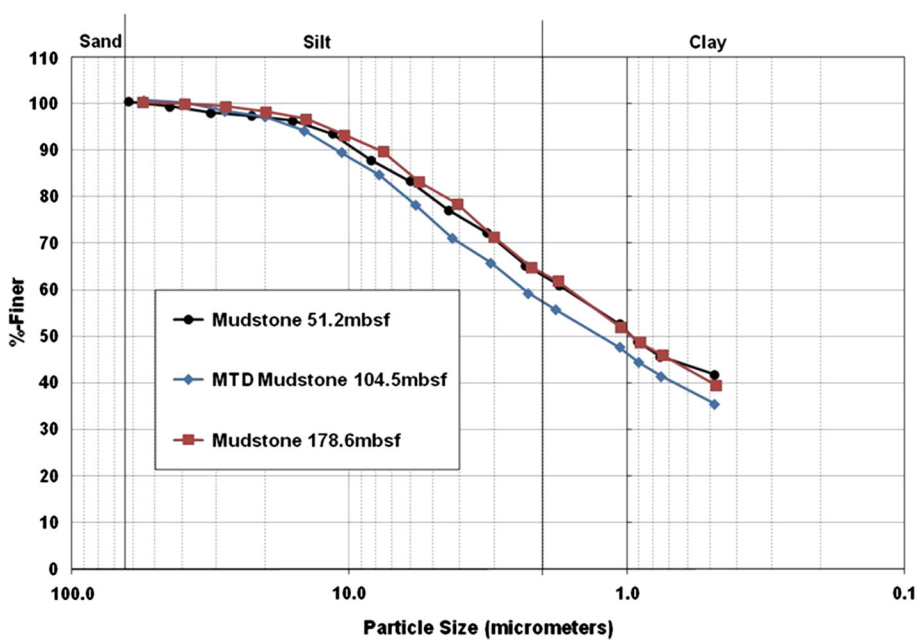

Fig. 5. Grain size curves for two mudstones and one MTD mudstone. The mudstones have very similar curves and the MTD mudstone is marginally coarser grained. These are the same samples used in Fig. 7 and their grain sizes make them silty clays (Shepard, 1954).

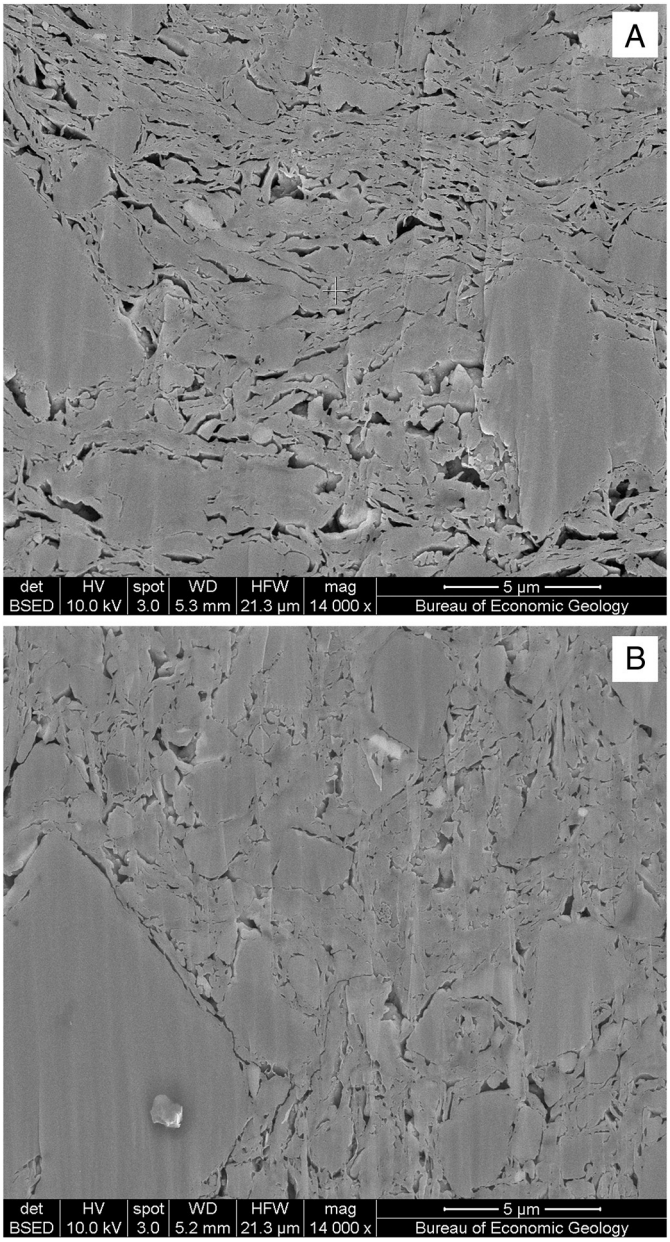

Fig. 6. Backscattered electron images on argon-ion milled surfaces, A) MTD mudstone and B) non-deformed mudstone (A = 104.5 mbsf; grain size = 57% clay size; MICP porosity = 36%; preferred orientation ranges 3.28 to 4.03 m.r.d.; B = 178.6 mbsf; grain size = 63% clay size; MICP porosity = 37%; preferred orientation ranges 2.53 to 2.68 m.r.d.).

displacement pressure (or closure-pressure), the point where 10% mercury has saturated the sample (the y-axis in Fig. 7 is cut at 10,000 psi to highlight this). We use Eq. (2) to convert mercury intrusion pressure to a pore throat size (e.g. x-axis of Fig. 7B). Next, using the first derivative of these curves we can express the pore throat size distributions as a probability density function, where we are able to see the differences between the samples even at the same porosity (Fig. 7B). Below 30 nm and above 200 nm the pore throat size distributions are quite similar and there is some noise in the 3–5 nm range that has not been smoothed out. The differences in the pore throat size distributions lie between 200 and 30 nm. The MTD mudstone has a tighter distribution with a greater concentration of pore throat sizes at ~50 nm than the mudstone sample. Interestingly, the modal pore throat size is approximately the same for both samples.

In the second case (Fig. 7C and D), the intrusion curves are significantly different with the shallower mudstone sample having a much lower 10% mercury saturation pressure. This is consistent with the differences in total porosity between the samples. The pore throat size distributions are very different between these samples (Fig 7D), where the MTD mudstone sample has a defined modal point the mudstone sample does not and has a very broad range of pore throat sizes with pore throats greater than 200 nm. No pore throat in the MTD mudstone is greater than ~100 nm. The total porosity differences and pore throat size distributions cannot be modeled with vertical effective stress differences, 0.14 MPa in the mudstone and 0.37 MPa in the MTD mudstone, and a pore compliance change with size (Emmanuel and Day-Stirrat, 2012). Therefore, the mechanism of generating these pore throat size differences is significantly different.

In the third case (Fig. 7E and F), Day-Stirrat et al. (2012) showed that an increase in vertical effective stress drove a decrease in porosity and a modification of the pore throat size distribution by a pore collapse mechanism that did not affect all pore throat sizes equally. Similar observations were confirmed through modeling exercises on grain size and stress controlled resedimented materials (Emmanuel and Day-Stirrat, 2012).

4. Discussion

Samples from Ursa allow a detailed study of the microfabric of mud-rich mass transport deposits. Mudstone samples from Ursa were the subject of study by Day-Stirrat et al. (2012) who showed a small increase in the preferred orientation of illite–smectite with increasing vertical effective stress. Samples from MTDs at both sites (Figs. 3 and 4) in this study show increased illite–smectite fabric intensities relative to this background reference frame. The mechanism that preferentially aligned clay particles at Ursa had significant effects on total porosity and pore throat size distributions (Fig. 7 and Table 1).

It is generally presumed that a flocculated clay aggregate is composed of randomly oriented clay particles (O'Brien, 1971) and thus has an “m.r.d.” equal to 1 (Fig. 8A). The deposition of flocs occurs at some critical aggregate size (Kranck, 1975; Kranck and Milligan, 1985; Kranck, 1991; Kranck et al., 1996). Clays in suspension in an electrolytic solution are governed by physio-chemical forces and flocs are formed when a balance is reached among attractive and repulsive interparticle forces and hydrodynamic forces. Attractive forces such as short range ‘van der Waals’ attraction and ‘edge-to-face’ electrical double layer interaction can induce the classic ‘card-house’ structure as imaged by O'Brien (1970, 1971).

After deposition, this flocculated clay particle arrangement is modified by vertical effective stress driven consolidation that can reduce porosity and reorganize microfabric (Day-Stirrat et al., 2012). Mass transport deposit samples exhibit a different porosity and microfabric modification process. Shipp et al. (2004) and Sawyer et al. (2009) proposed that during slope failure the affected sediment is remolded causing a sediment density increase; primary evidence for this is porosity reduction through an MTD (Figs. 3 and 4) and increased resistivity response (Dugan, 2012). At the particle contact point, remolding is a shearing action where inter-particle forces are overcome and mechanical locking is undone. This allows platy particles to slide past each other and cause a reordered microfabric (Fig. 8B), aligning particles in the same way that synthetically consolidated montmorillonite was sheared and aligned in the laboratory (Haines et al., 2009) and clay gouge may be aligned in fault zones (Solum et al., 2003; Solum et al., 2005; Haines et al., 2009). Backscattered images from Ursa (Fig. 6) show the response of the sediment to the action of shear. The MTD mudstone has a well aligned clay microfabric. Based on resisitivity increase and porosity reduction it appears that sediment density increases towards the base of MTDs (Figs. 3 and 4). However, an increase in illite–smectite fabric intensity

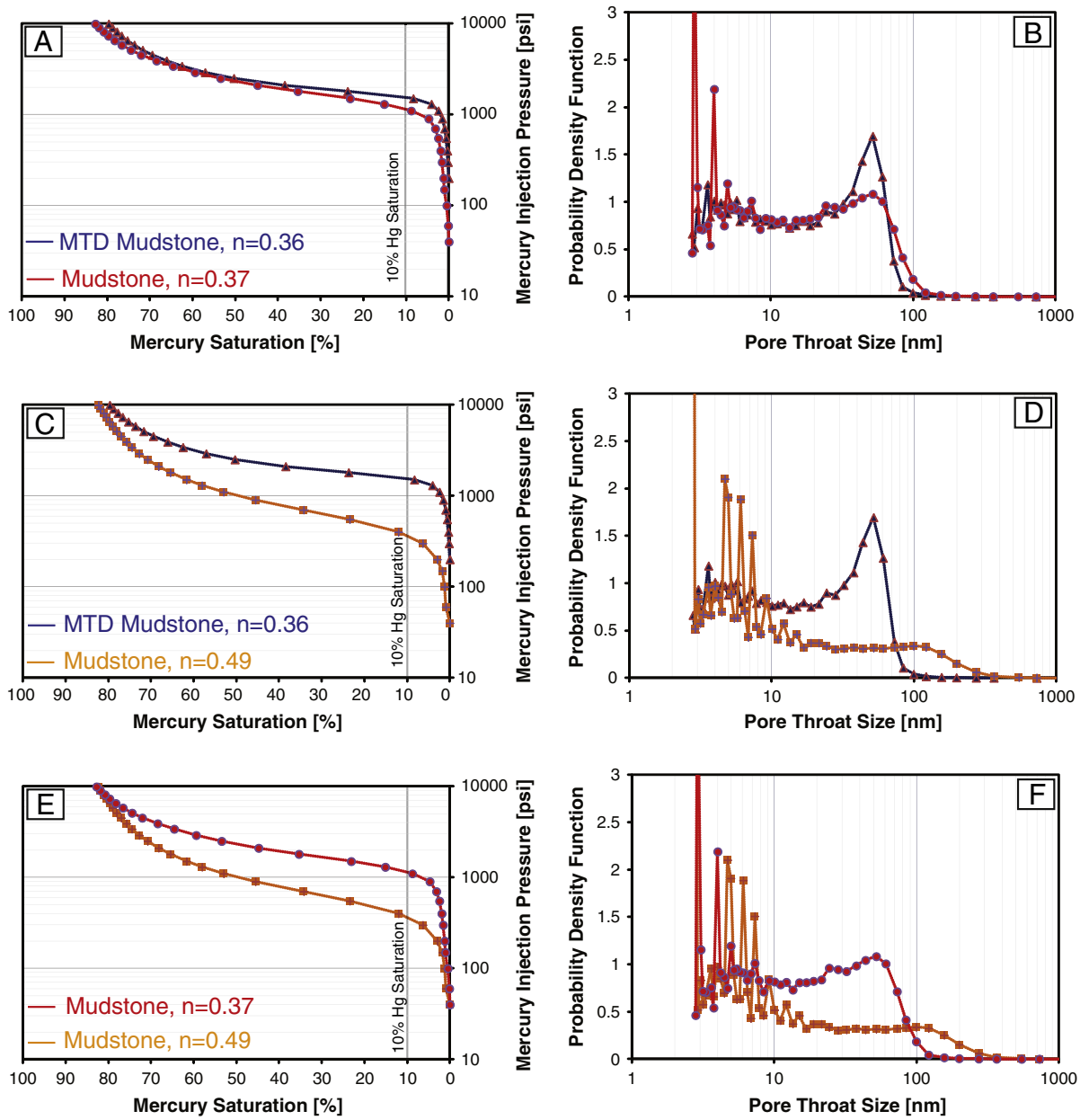

Fig. 7. Cumulative mercury injection curves (A) for a conventional mudstone and an MTD mudstone (Table 1) at similar porosities but different depths, MTD is at 104.5 mbsf and the mudstone is at 178.6 mbsf and (B) pore throat size distributions. Cumulative mercury injection curves (C) and pore throat size distributions (D) for a conventional mudstone (51.2 mbsf) and an MTD mudstone (104.5 mbsf), differences are not governed by vertical effective stress differences. Cumulative saturation curves (E) and pore size distributions (F) for a conventional mudstone (51.2 mbsf) and an MTD mudstone (178.6 mbsf) governed by vertical effective stress differences. n = porosity.

does not always correlate with an increase in sediment density (Fig. 4), although this is the case at U1324 (Fig. 3). It should be noted that preferred orientation measurements are carried out on the millimeter scale and MTD-2, where this comparison is made, is ~50 m thick (Sawyer et al., 2009) and so local heterogeneity cannot be controlled.

In the case where phyllosilicate fabric intensity is controlled by vertical effective stress it is possible to be somewhat predictive at a given depth (vertical effective stress). In MTD mudstones it is not possible to be nearly as predictive because phyllosilicate fabric intensity does not increase with vertical effective stress, but it is possible to say that phyllosilicates in MTD mudstones will have a greater preferred orientation (by 0.5 to 1.0 m.r.d) than a conventional mudstone of the same composition at a similar depth (vertical effective stress). The Ursa samples cover a maximum burial depth of ~600 mbsf but other studies (Ho et al., 1999; Day-Stirrat et al., 2008) have recorded burial diagenetic fabric intensities to ~7000 m. These deeply buried samples have undergone mineral transformations that have enhanced the alignment of clays in their microfabric (Ho et al., 1999; Day-Stirrat et al., 2008). The MTD mudstone samples at Ursa have implications for how these results are interpreted in deeper and hotter parts of basins. The enhanced preferred orientations developed through slope failure and shearing mechanisms will be carried into the diagenetic zone and will probably result in even further enhanced fabric intensities and will have an effect on how the rock behaves in response to a propagating sound wave and how anisotropic it may be (Banik, 1984; Vernik and Liu, 1997; Domnesteanu et al., 2002; Kanitpanyacharoen et al., 2011).

To consolidate mudstones at Ursa from 49% porosity to 36% porosity, in the absence of shearing, vertical effect stress removes the

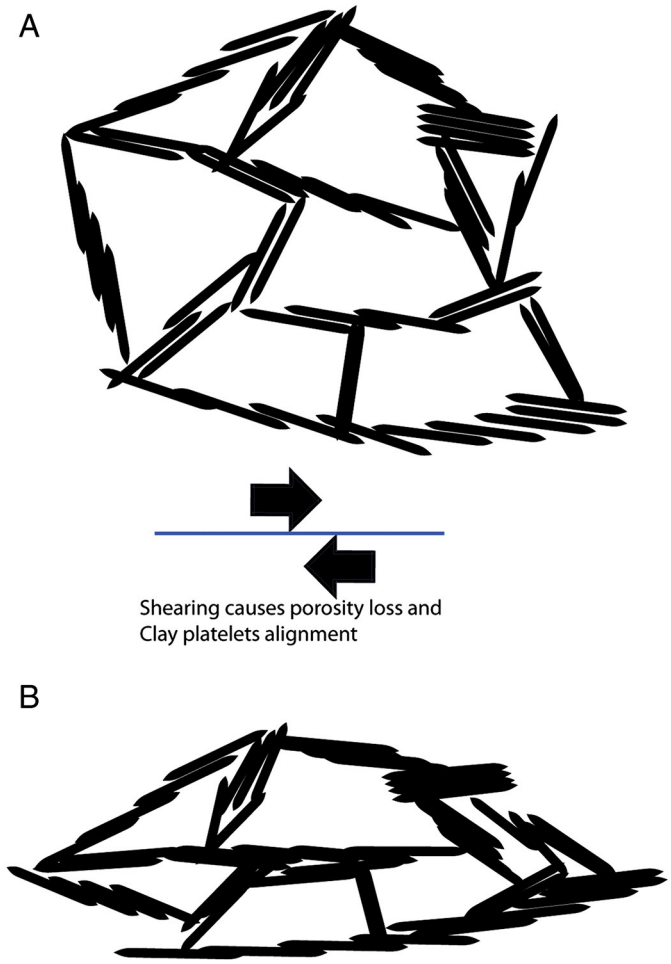

Fig. 8. Illustration of a floc with clay platelets in face-to-face and edge-to-face morphologies (A). Remolding during deposition of a mass transport deposit breaks original floc strictures increasing clay mineral preferred orientations and decreasing porosity (B).

largest pore throat sizes (Fig. 7F) and modifies the distribution of smaller pore throat sizes (Fig. 7E and F) while marginally rotating platy clay minerals (Day-Stirrat et al., 2012). This process, naturally, modifies the sealing capacity (column height in Table 1) of a mudstone, with sealing capacity increasing with porosity reduction (increased depth) as it becomes increasingly hard to inject a non-wetting phase into smaller and smaller pore throat sizes. The general effects in MTD mudstones are a reduction of both large pores and mean pore size relative to depth equivalent mudstone samples (Fig. 7). Remolding has significantly altered the response of the sediment to mercury intrusion, and by extension any non-wetting phase. We calculated theoretical column heights (Schowalter, 1979; Schlomer and Krooss, 1997) for oil and gas from mercury injection capillary pressure (MICP) data. We made the calculation at 10% mercury saturation and assumed an oil–water surface tension of 0.035 N/m; gas–water surface tension of 0.042 N/m; the oil–water–mineral and gas–water–mineral contact angle of 180°; and oil, gas and water densities of 800, 240 and 1095 kg/m^2 respectively. Calculated membrane-limited column heights (Table 1) for oil and gas suggest that at shallow depths an MTD mudstone at 104.5 mbsf will seal ~4.8 times better than a mudstone at 51.2 mbsf (439 m of oil versus 90 m). Similarly, an MTD mudstone with 36% porosity will seal ~1.3 times better than a mudstone at 37% porosity that is buried ~70 m deeper (439 m of oil versus 329 m). These observations have significant implications for the rate of fluid flow in the shallow section and the development and dissipation of excess pore pressure.

Field curves of consolidation have long been studied from the perspective of the decline in porosity. Our contribution is to show that porosity loss in the shallow section may occur through more than one mechanism (i.e. compaction) and that the different porosity loss mechanisms have significant impacts on the microfabric of the sediment. The micofabric in turn controls the likelihood of particle induced permeability anisotropy by the introduction of tortuosity to flow in seemingly unlikely situations. On a sample scale, we interpret the remolding of sediment in an MTD deposit to do two things; 1) align clay platelets and align and elongate pores (Figs 5 and 7); 2) it preferentially destroys large pores and creates a pore size distribution that is more monomodal and uniform in comparison to a mudstone sample at a similar burial depths. Therefore, these physical property changes should have an impact on velocity, strength behavior and permeability.

5. Conclusions

MTD mudstones have higher fabric intensities than compositional equivalent mudstones either at a given porosity or a given depth as quantified by HRXTG and imaged using argon-ion milling and BSE imaging. Enhanced clay-mineral fabric intensities in MTD mudstones are interpreted to result from remolding and shearing after deposition, where clay mineral flocs have been mechanically disaggregated and physio-chemical forces of attraction overcome. The enhanced clay mineral fabric intensities are then carried into deeper burial regimes. Recognition of enhanced clay mineral fabric intensities has important implications for seismic anisotropy in the deep subsurface. Increased mercury entry pressures in shallow buried MTD mudstones relative to compositionally equivalent mudstones represent a barrier to fluid flow even at depths of <150 mbsf.

Acknowledgments

We thank the UT Geofluids Industrial Associates Program for their sponsorship and the scientists of IODP Expedition Leg 308. MICP measurements were made at Newcastle University UK. HRXTG is supported by EMAL at the University of Michigan and NSF grant EAR-0345985 to Ben van der Pluijm. This research builds on insights derived from samples and/or data provided by the Integrated Ocean Drilling Program (IODP). The IODP is sponsored by the U.S. National Science Foundation (NSF) and participating countries. Constrictive and insightful reviews by Dr. Neil Goulty and Dr. Samuel Haines significantly improved the final manuscript.

References

Arnould, M., Audiguier, M., Delage, P., Pellerin, F.-M., Struillou, R., Vayssade, B., 1980. Etude des sols argileux par la porosimétrie au mercure. Contrôle des variations de texture sous diverses conditions. International Association of Engineering Geologists Bulletin, 22 213–223.

ASTM, 2007. Standard test method for particle-size analysis of soils. In: International, A.D 422-63. West Conshohocken, PA. p. 8.

Banik, N.C., 1984. Velocity anisotropy of shales and depth estimation in the North-Sea Basin. Geophysics 49 (9), 1411–1419.

Burland, J.B., 1990. 30th Rankine lecture — on the compressibility and shear-strength of natural clays. Geotechnique 40 (3), 329–378.

Dan, G., Sultan, N., Savoye, B., 2007. The 1979 Nice harbour catastrophe revisited: trigger mechanism inferred from geotechnical measurements and numerical modelling. Marine Geology 245 (1–4), 40–64.

Day-Stirrat, R.J., Aplin, A.C., Srodon, J., van der Pluijm, B.A., 2008. Diagenetic reorientation of phyllosilicate minerals in Paleogene mudstones of the Podhale Basin, southern Poland. Clays and Clay Minerals 56 (1), 100–111.

Day-Stirrat, R.J., Flemings, P.B., You, Y., Aplin, A.C., van der Pluijm, B.A., 2012. The fabric of consolidation in Gulf of Mexico mudstones. Marine Geology 295–298, 77–85.

Delage, P., Lefebvre, G., 1984. Study of the structure of a sensitive Champlain clay and of its evolution during consolidation. Canadian Geotechnical Journal 21 (1), 21–35.

Domnesteanu, P., McCann, C., Sothcott, J., 2002. Velocity anisotropy and attenuation of shale in under- and overpressured conditions. Geophysical Prospecting 50 (5), 487–503.

Dugan, B., 2012. Petrophysical and consolidation behavior of mass transport deposits from the northern Gulf of Mexico, IODP Expedition 308. Marine Geology 315–318, 98–107.

Emmanuel, S., Day-Stirrat, R.J., 2012. A framework for quantifying size dependent deformation of nano-scale pores in mudrocks. Journal of Applied Geophysics 86, 29–35.
Flemings, P.B., Behrmann, J.H., John, C.M., the Expedition 308 Scientists, 2006. Proc. IODP, 308. Integrated Ocean Drilling Program Management International, Inc., College Station TX. http://dx.doi.org/10.2204/iodp.proc.308.101.2006.
Fryer, G.J., Watts, P., Pratson, L.F., 2004. Source of the great tsunami of 1 April 1946: a landslide in the upper Aleutian forearc. Marine Geology 203 (3–4), 201–218.
Garziglia, S., Migeon, S., Ducassou, E., Loncke, L., Mascle, J., 2008. Mass-transport deposits on the Rosetta province (NW Nile deep-sea turbidite system, Egyptian margin): characteristics, distribution, and potential causal processes. Marine Geology 250 (3–4), 180–198.
Haines, S.H., van der Pluijm, B.A., Ikari, M.J., Saffer, D.M., Marone, C., 2009. Clay fabric intensity in natural and artificial fault gouges: implications for brittle fault zone processes and sedimentary basin clay fabric evolution. Journal of Geophysical Research — Solid Earth 114.
Hildenbrand, A., Urai, J.L., 2003. Investigation of the morphology of pore space in mudstones-first results. Marine and Petroleum Geology 20 (10), 1185–1200.
Ho, N.C., Peacor, D.R., van der Pluijm, B.A., 1999. Preferred orientation of phyllosilicates in Gulf Coast mudstones and relation to the smectite–illite transition. Clays and Clay Minerals 47 (4), 495–504.
Jenner, K.A., Piper, D.J.W., Campbell, D.C., Mosher, D.C., 2007. Lithofacies and origin of late Quaternary mass transport deposits in submarine canyons, central Scotian Slope, Canada. Sedimentology 54 (1), 19–38.
John, C.M., Adatte, T., 2009. Data Report: X-Ray Analyses of Bulk Sediment in IODP Holes U1320A and U1324B, Northern Gulf of Mexico. In: Flemings, P.B., Behrmann, J.H., John, C.M., the Expedition 308 Scientists (Eds.), Proc. IODP, 308. Integrated Ocean Drilling Program Management International, Inc., College Station, TX.
Kanitpanyacharoen, W., Wenk, H.-R., Kets, F., Lehr, C., Wirth, R., 2011. Texture and anisotropy analysis of Qusaiba shales. Geophysical Prospecting 59 (3), 536–556.
Kranck, K., 1975. Sediment deposition from flocculated suspensions. Sedimentology 22 (1), 111–123.
Kranck, K., Milligan, T.G., 1985. Origin of grain-size spectra of suspension deposited sediment. Geo-Marine Letters 5 (1), 61–66.
Kranck, K., 1991. Interparticle grain size relationships resulting from flocculation. In: Bennett, R.H., Bryant, W.R., Hulbert, M.H. (Eds.), Microstructure of Fine-Grained Sediments. Springer Verlag, pp. 125–130.
Kranck, K., Smith, P.C., Milligan, T.G., 1996. Grain-size characteristics of fine-grained unflocculated sediments.1. 'One-round' distributions. Sedimentology 43 (3), 589–596.
Long, H., Flemings, P.B., Germaine, J.T., Saffer, D.M., 2011. Consolidation and overpressure near the seafloor in the Ursa Basin, Deepwater Gulf of Mexico. Earth and Planetary Science Letters 305 (1–2), 11–20.
Loucks, R.G., Reed, R.M., Ruppel, S.C., Jarvie, D.M., 2009. Morphology, genesis, and distribution of nanometer-scale pores in siliceous mudstones of the Mississippian Barnett Shale. Journal of Sedimentary Research 79 (11–12), 848–861.
Lowell, S., Shields, J.E., 1984. Powder Surface Area and Porosity, second ed. Wiley, New York.
McMurtry, G.M., Watts, P., Fryer, G.J., Smith, J.R., Imamura, F., 2004. Giant landslides, mega-tsunamis, and paleo-sea level in the Hawaiian Islands. Marine Geology 203 (3–4), 219–233.
Meissl, S., Behrmann, J., Behrmann, J.H., 2010. Data report: preliminary assessment of Pleistocene sediment strength in the Ursa Basin (Gulf of Mexico continental slope) from triaxial and ring shear test data. Proceedings of the Integrated Ocean Drilling Program 308. http://dx.doi.org/10.2204/iodp.proc.308.211.2010.
Forsberg, C.F., Locat, J., 2005. Mineralogical and microstructural development of the sediments on the Mid-Norwegian margin. Marine and Petroleum Geology 22 (1–2), 109–122.
Mitchell, J.K., Soga, K., 2005. Fundamentals of Soil Behavior. John Wiley & Sons Inc.
Moscardelli, L., Wood, L., Mann, P., 2006. Mass-transport complexes and associated processes in the offshore area of Trinidad and Venezuela. American Association of Petroleum Geologists Bulletin 90 (7), 1059–1088.
Moscardelli, L., Wood, L., 2008. New classification system for mass transport complexes in offshore Trinidad. Basin Research 20 (1), 73–98.
O'Brien, N.R., 1970. The fabric of shale — an electron microscope study. Sedimentology 15, 229–246.
O'Brien, N.R., 1971. Fabric of kaolinite and illite floccules. Clays and Clay Minerals 19, 353–359.
Pickering, K.T., Corregidor, J., 2005. Mass-transport complexes, (MTCs) and tectonic control on basin-floor submarine fans, middle Eocene, south Spanish Pyrenees. Journal of Sedimentary Research 75 (5), 761–783.
Piper, D.J.W., Pirmez, C., Manley, P.L., Long, D., Flood, R.D., Normark, W.R., Showers, W., 1997. Mass-transport deposits of the Amazon Fan. In: Flood, R.D., Piper, D.J.W., Klaus, A., Peterson, L.C. (Eds.), Proc. ODP, Sci. Results. Ocean Drilling Program, College Station, TX, pp. 109–146.
Romero, E., Simms, P., 2008. Microstructure investigation in unsaturated soils: a review with special attention to contribution of mercury intrusion porosimetry and environmental scanning electron microscopy. Geotechnical and Geological Engineering 26 (6), 705–727.
Sawyer, D.E., Jacoby, R., Flemings, P.B., Germaine, J.T., 2008. Data Report: Particle Size Analysis of Sediments in the Ursa Basin, IODP Expedition 308 Site U1324 and U1322, Northern Gulf of Mexico. In: Flemings, P.B., John, C. (Eds.), Proceedings of the Integrated Ocean Drilling Program, Scientific Results, p. 308.
Sawyer, D.E., Flemings, P.B., Dugan, B., Germaine, J.T., 2009. Retrogressive failures recorded in mass transport deposits in the Ursa Basin, Northern Gulf of Mexico. Journal of Geophysical Research — Solid Earth 114.
Schlomer, S., Krooss, B.M., 1997. Experimental characterisation of the hydrocarbon sealing efficiency of caprocks. Marine and Petroleum Geology 14, 565–580.
Schowalter, T.T., 1979. Mechanics of secondary hydrocarbon migration and entrapment. American Association of Petroleum Geologists Bulletin 63 (5), 723–760.
Shepard, F.P., 1954. Nomenclature based on sand–silt–clay ratios. Journal of Sedimentary Petrology 24, 151–158.
Shipp, C., Nott, J.A., Newlin, J.A., 2004. Physical characteristics and impact of mass transport complexes on deepwater jetted conductors and suction anchor piles. Offshore Technology Conference, Houston, Texas, p. 11.
Sintubin, M., 1995. High-resolution X-ray texture goniometry: discussion. Journal of Structural Geology 17 (6), 923–924.
Skempton, A.W., 1970. The consolidation of clays by gravitational compaction. Quarterly Journal of the Geological Society of London 125, 373–411.
Solum, J.G., van der Pluijm, B.A., Peacor, D.R., Warr, L.N., 2003. Influence of phyllosilicate mineral assemblages, fabrics, and fluids on the behavior of the Punchbowl Fault, southern California. Journal of Geophysical Research — Solid Earth 108 (B5).
Solum, J.G., van der Pluijm, B.A., Peacor, D.R., 2005. Neocrystallization, fabrics and age of clay minerals from an exposure of the Moab Fault, Utah. Journal of Structural Geology 27 (9), 1563–1576.
Stow, D.A.A., 1986. Deep clastic seas. Sedimentary Environments and Facies.Blackwell Scientific Publications, Oxford (399–444 pp.).
Tappin, D.R., Watts, P., McMurtry, G.M., Lafoy, Y., Matsumoto, T., 2001. The Sissano, Papua New Guinea tsunami of July 1998 — offshore evidence on the source mechanism. Marine Geology 175 (1–4), 1–23.
Tripsanas, E.K., Piper, D.J.W., Jenner, K.A., Bryant, W.R., 2008. Submarine mass-transport facies: new perspectives on flow processes from cores on the eastern North American margin. Sedimentology 55 (1), 97–136.
van der Pluijm, B.A., Ho, N.-C., Peacor, D.R., 1994. High-resolution X-ray texture goniometry. Journal of Structural Geology 16, 1029–1032.
van der Pluijm, B.A., Ho, N.-C., Peacor, D.R., 1995. High-resolution X-ray texture goniometry: reply. Journal of Structural Geology 17 (6), 925–926.
Vernik, L., Liu, X.Z., 1997. Velocity anisotropy in shales: a petrophysical study. Geophysics 62 (2), 521–532.
Washburn, E.W., 1921. Note on a method of determining the distribution of pore sizes in a porous material. Proceedings of the National Academy of Science, Bulletin 63, 723–760.
Weimer, P., Shipp, C., 2004. Mass transport complex: musing on past uses and suggestions for future directions, OTC paper 16752. Paper Presented at Offshore Technology Conference, Houston, Texas, USA.
Wenk, H.R., 1985. Measurement of pole figures. In: Wenk, H.R. (Ed.), Preferred Orientation in Deformed Metals and Rocks: An Introduction to Modern Texture Analysis. Academic Press Inc., pp. 11–48.